A scaling law approach to rate fabrication tolerances of double-sided electrostatic actuators
Supplement

Franziska Wall, Hermann A. G. Schenk, Anton Melnikov and Bert Kaiser

Contents

1 General modeling approaches

Continuum model

- Force equilibrium / Newton method
- Energy conservation / Hamilton's principle

Equation of Motion, Boundary conditions

- e.g. Euler-Bernoulli equation for a clamped-free beam (compare e.g. [1])

$$E \cdot I \cdot \frac{\partial^4 w}{\partial x^4} + \rho b h \frac{\partial^2 w}{\partial t^2} = \frac{1}{2} \epsilon b \frac{V^2}{(d-w)^2} \tag{1}$$

$$w(0,t) = 0, \frac{\partial w(0,t)}{\partial \xi} = 0, \frac{\partial^3 w(l,t)}{\partial \xi^3} = 0, \frac{\partial^2 w(l,t)}{\partial \xi^2} = 0 \tag{2}$$

Nondimensionalization [2]

- Compact modeling: Connection of universal parameters to geometry parameters
- Meaning of small/large numbers; Neglecting terms, approximations and numerical treatment
- Universal equations with less dependency on concrete geometry/system (e.g. [3])
- e.g. voltage scaling in [4], [5], [1]

$$u = U\sqrt{\alpha_2} = U \cdot \sqrt{\frac{6\epsilon L^4}{E h^3 d^3}} \tag{3}$$

Order-reduction

- Separation of spatial and time-domain
- e.g. Galerkin projection towards eigenmodes [5]

$$w(\tau, \xi) = \sum_{n=0}^{N} a(\tau) \cdot \psi_n(\xi) \tag{4}$$

Figure 1: Common analysis of actuators

2 Modeling a push-pull nano-e-drive (NED) actuator

In this section the lumped parameter model (LPM) of the push-pull nano-e-drive (NED) actuator and its motivation is summarized (sec. 2.1 and 2.2). In the following the impact of a symmetric gap variation on the stability (sec. 2.3) and the scaling of dimensionless quantities (sec. 2.4)is evaluated for the reference model. Last, the reference model with a gap asymmetry is analysed (sec. 2.5)

2.1 Lumped parameter model (LPM)

A more general lumped parameter model for a push-pull NED actuator (fig. 3) with the model parameters in table 1 was motivated in [6]:

$$\frac{d^2}{d\tau^2}a + \frac{1}{Q}\frac{d}{d\tau}a + a = \Theta_1(u_1)\left(\frac{u_1}{\gamma_1(u_1,a) - a}\right)^2 - \Theta_2(u_2)\left(\frac{u_2}{\gamma_2(u_2,a) + a}\right)^2, \tag{5}$$

with the generalized dergee-of-freedom a, the quality factor Q, the effective gaps γ_1 and γ_2, the leverage factors Θ_1 and Θ_2 for each actuator layer, the dimensionless time τ as well as the dimensionless voltages u_1 and u_2 in the upper and lower actuator layer, respectively. The scaling of the voltage is connected to the static pull-in voltage,

$$\begin{aligned} u &= \frac{U}{U_0}, \\ U_0 &= u_{\mathrm{PI}}^{-1} \cdot U_{\mathrm{PI}}. \end{aligned} \tag{6}$$

Thereby, the dimensionless pull-in voltage of equation 5 is u_{PI} and pull-in voltage with dimensions is U_{PI}. The dimensionless voltages are chosen as a differential driving with an asymmetric detuning $\hat{\delta}_u$ of the bias voltage u_{dc},

$$\begin{aligned} u_1 &= u_{\mathrm{dc}} \cdot (1 + \hat{\delta}_u) + u_{\mathrm{s}}, \\ u_2 &= u_{\mathrm{dc}} \cdot (1 - \hat{\delta}_u) - u_{\mathrm{s}}. \end{aligned} \tag{7}$$

For a single-tone excitation the signal voltage u_{s} is

$$u_{\mathrm{s}} = u_{\mathrm{ac}} \cos \nu\tau \tag{8}$$

with the dimensionless frequency ν. For the low-frequency limit ($\nu \to 0$) $\hat{\delta}_u$ is mathematically equivalent to $\mathfrak{u}_{\mathrm{ac}} u_{\mathrm{dc}}$. The single-sided drive with only one active layer refers to $u_{\mathrm{s}} = 0$ and $\hat{\delta}_u = \pm 1$. A symmetric drive with both layers equally activated is realized by $u_1 = u_2$. The effective capacitor gap γ_i is influenced by the motion of the outer electrodes (e.g. by $\sim g_u u_i^2$) as well as the dimensionless deflection a, which is related to the deformation of the electrodes by the actuator deflection. For this push-pull NED actuator, the gap change by the motion of the outer electrodes in stationary 2D-FEM simulations is small ($\lessapprox 0.6\%$ of the initial gap for a symmetric drive and $\lessapprox 0.2\%$ of the initial gap for a single-sided drive) compared to the change by the deflection of the middle electrode ($\lessapprox 30\%$ of the initial gap for a single-sided drive). Additionally, the terms proportional to g_u and g_a counteract each other for a non-symmetric drive. Thus, a model with $g_u = 0$ and $g_a = 0$ is used.

$$\begin{aligned} \gamma_1(u_1,a) &= 1 - g_{\mathrm{u}} \cdot u_1^2 - g_{\mathrm{a}} \cdot u_1^2 \cdot a \approx 1, \\ \gamma_2(u_2,a) &= 1 - g_{\mathrm{u}} \cdot u_2^2 + g_{\mathrm{a}} \cdot u_2^2 \cdot a \approx 1. \end{aligned} \tag{9}$$

Motivation of generalized ansatz [6]

- dimensionless equations from common analysis
- observations combined with effective models like spring-plate-models
- crucial behaviour, e.g. bifurcation types or symmetry

Linking dimensionless parameters to physical response [6]

- here: Scaling of the generalized degree-of-freedom a by Θ and voltage scaling by U_0 for the ideal geometry
- non-destructive estimation of U_0 and Θ with an electro-acoustic method by harmonic distortion analysis [6]
- comparison to FEM-simulations/ experimental data to judge: Is the generalized ansatz precise enough or is an extension necessary?
  e.g. singularity structure of the electrostatic force: $\sim \mathrm{gap}^{-2}$ by a spring-plate model or motivated by a single-mode approximation of the euler-bernoulli-beam equation as $\sim a + b \cdot \mathrm{gap}^{-1/2} + c \cdot \mathrm{gap}^{-3/2}$ [7] with constants a,b,c.

Connecting universal parameters to geometry [8]

- Connection between geometry variations and change of bifurcation position
  $\rightarrow$ additional scaling parameters Υ_u, Υ_x
- here: FEM-simulations of single-sided pull-in for Υ_u and Υ_x
- adjustment of the generalized ansatz if necessary, e.g. here to treat asymmetric fabrication tolerances

Figure 2: Dimensional analysis used in [6] and this publication

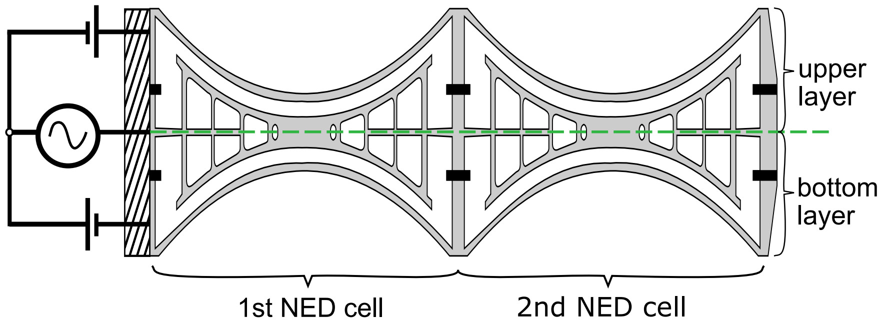

Figure 3: Scheme of the push-pull NED actuator [6] reproduced with premission from Springer Nature

Further, a leverage factor translates the motion of the middle electrode into the tip deflection. The motion of the middle electrode an the tip deflection is qualitatively comparable for FEM-simulations as well as optical measurements [10]. With a single-sided drive, the voltage dependency of the leverage factor was studied by the relation between the tip deflection and the gap within the passive layer. The voltage difference is zero for this passive layer. The linear term $\sim u$ is zero. The leverage factor does not depend on the voltage polarity, due to the u^2-dependency of the electrostatic force. The quadratic term $\sim u^2$ is already five orders of magnitudes lower than the constant coefficient. Consequently, the leverage factor is assumed constant with respect to the applied voltage,

$$\Theta_1(u_1) = \Theta_2(u_2) \approx 1. \tag{10}$$

Thus, the voltage scaling U_0 in equation 6 is

$$U_0(g_u = 0, g_a = 0) = 2 \cdot U_{\mathrm{PI}}. \tag{11}$$

A more extended argumentation about the LPM can be found in [6], Online Source 4.

2.2 Analysis of a reference model

Here, we summarize the reference model to motivate the dimensionless equation of motion (eq. 5) for the push-pull NED actuator (Fig. 3) and discuss later the relation to the pull-in. The two capacitors in the upper layer are in parallel and assumed thus as one effective capacitor. Likewise the lower layer is modelled as a second effective capacitor. Each cell consists out of three moveable electrodes. Figure 4 displays a LPM for this situation, where the voltages U_1 and U_2 are applied at the upper and lower electrode, respectively. Each electrode has a linear stiffness k_i and deflects by x_i. The indices 1, 2 and 3 refer to the upper, the middle and the lower electrode, respectively. The initial gap is g_0 and the capacitors area is A. The relative permittivity is ϵ_r and ϵ_0 is the dielectric constant. The potential energy V is the summation of the elastic energy and the electrostatic potential, which is modelled by the equation of a parallel plate capacitor,

$$V = \frac{1}{2}k_1 x_1^2 + \frac{1}{2}k_2 x_2^2 + \frac{1}{2}k_3 x_3^2 - \frac{1}{2}A\epsilon_0\epsilon_r \left(\frac{U_1^2}{g_0 + x_1 - x_2} + \frac{U_2^2}{g_0 + x_2 - x_3} \right). \tag{12}$$

The potential energy by the linear coupling springs in figure 4 b is given by

$$V_{\mathrm{coupling}} = \frac{1}{2}k_0 \left(x_1 - x_2\right)^2 + \frac{1}{2}k_0 \left(x_2 - x_3\right)^2. \tag{13}$$

parameter	interpretation	note
a	Dimensionless degree-of-freedom (see sec. 3)	
τ	Dimensionless time	
Q	Quality factor	highspeed camera measurement ($Q \approx 3.9$ [9])
u_{dc}	dimensionless bias voltage	
u_s	dimensionless signal voltage	
u_{PI}	dimensionless DC pull-in for a symmetric drive	$u_{PI}(g_u = 0, g_a = 0) = 0.5$
U_{PI}	DC pull-in for a symmetric drive	low frequency distortions with symmetric and asymmetric driving
Θ	Leverage factor	stationary FEM simulation: constant
g_u	voltage-induced gap reduction	modal FEM: $g_u = 0.97$
g_a	gap change by beam deflection	stationary FEM with single-sided drive: counteracts $g_u \Rightarrow g_u = 0, g_a = 0$
$\hat{\delta}_u$	asymmetric deviation of the bias voltage compared to the mean bias	
$\tilde{\delta}_g$	symmetric deviation of the gap compared to the mean gap	
$\hat{\delta}_g$	asymmetric deviation of the gap compared to the mean gap	
U_0	voltage scaling	$U_0 = \frac{U_{PI}}{u_{PI}}$
X_0	length scaling	$X_0 = \frac{X_{PI}}{a_{PI}}$
T_0	time scaling	$T_0 = \frac{t}{\tau}$ (Needs some further strategy)
Υ_u	voltage scaling by symmetric fabrication tolerances	$\Upsilon_u = \frac{U_{PI}(\tilde{\delta}_g)}{U_{PI}(\tilde{\delta}_g = 0)}$
Υ_x	length scaling by symmetric fabrication tolerances	$\Upsilon_u = \frac{X_{PI}(\tilde{\delta}_g)}{X_{PI}(\tilde{\delta}_g = 0)}$

Table 1: Overview of the model parameters [6]

The dimensionless equation of motion is constructed similarly to e.g. [11]

$$\begin{aligned} &\xi_i = \frac{x_i}{g_0},\ \mathfrak{K} = \frac{k_1}{k_2} = \frac{k_3}{k_2}, \\ &u_i = \frac{U_i}{U_0},\ U_0 = \sqrt{\frac{2g_0^3 k_2}{A\epsilon_0\epsilon_r}} \text{ and} \\ &\psi = \frac{V}{g_0^2 k_2}. \end{aligned} \tag{14}$$

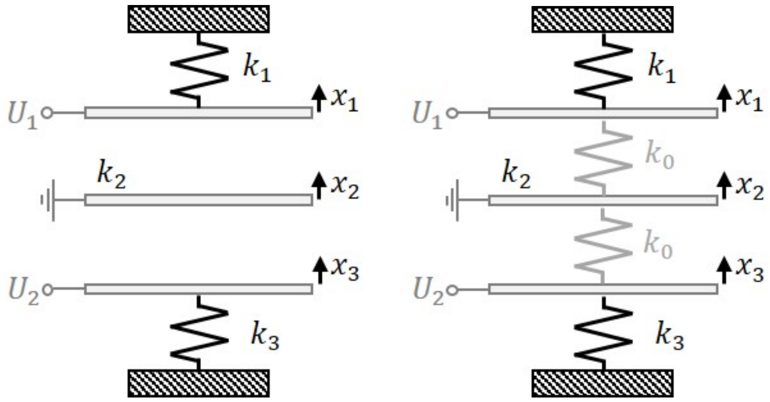

Figure 4: Reference model [6] reproduced with premission from Springer Nature

For the dimensionless deflection ξ_i the deflection x_i is set in relation to the initial gap g_0. The dimensionless potential becomes

$$\psi = \mathfrak{K}\frac{\xi_1^2}{2} + \frac{\xi_2^2}{2} + \mathfrak{K}\frac{\xi_3^2}{2} - \left(\frac{u_1^2}{1+\xi_1-\xi_2} + \frac{u_2^2}{1+\xi_2-\xi_3}\right) \tag{15}$$

and

$$\psi_{\text{coupling}} = \frac{1}{2}\kappa\left(\xi_1-\xi_2\right)^2 + \frac{1}{2}\kappa\left(\xi_2-\xi_1\right)^2. \tag{16}$$

The gap change by the electrode motion is

$$\Delta\mathfrak{g}_1 = \xi_1 - \xi_2, \tag{17}$$

$$\Delta\mathfrak{g}_2 = -\xi_3 + \xi_2. \tag{18}$$

The reaction forces at the three electrodes without coupling are calculated by the derivative of the potential energy,

$$\begin{pmatrix} F_1 \\ F_2 \\ F_3 \end{pmatrix} = \begin{pmatrix} \frac{\partial\psi}{\partial\xi_1} \\ \frac{\partial\psi}{\partial\xi_2} \\ \frac{\partial\psi}{\partial\xi_3} \end{pmatrix} = \begin{pmatrix} \mathfrak{K}\xi_1 + \frac{u_1^2}{(1+\xi_1-\xi_2)^2} \\ \xi_2 - \frac{u_1^2}{(1+\xi_1-\xi_2)^2} + \frac{u_2^2}{(1+\xi_2-\xi_3)^2} \\ \mathfrak{K}\xi_3 - \frac{u_2^2}{(1+\xi_2-\xi_3)^2} \end{pmatrix} = 0. \tag{19}$$

The forces at the outer electrodes, F_1 and F_3, are similar to the equation for a spring-plate model with one moveable electrode ξ_1 or ξ_3, respectively, with a stiffness modified by $\mathfrak{K}$ and a gap, that depends on the deflection of the middle electrode ξ_2. Stable solutions are given by

$$\xi_j = \varsigma_i\left(\frac{2}{3}\gamma_i - \frac{2}{3}\gamma_i \text{Cos}\left(\frac{2}{3}\text{Arcsin}\left(\frac{3}{2}\sqrt{\frac{3}{\mathfrak{K}\gamma_i^3}}u_i\right)\right)\right) \tag{20}$$

with $\gamma_1 = 1-\xi_2$ and $\varsigma_1 = -1$ for analyzing ξ_1 and $\varsigma_2 = +1$ and $\gamma_2 = 1+\xi_2$ for analyzing ξ_3 (trigonometric solution of a cubic equation, François Viète). These equations can be inserted in F_2, but they are rather complex. Thus, a series expansion around small voltages u_i followed by a second series approximation around small deflections ξ_2,

$$\xi_j \approx \varsigma_i \cdot \mathfrak{K}^{-1}u_i^2 \tag{21}$$

gives an estimation for the impact on the gap $\mathfrak{g}_i$ by the motion of the outer electrodes,

$$
\begin{aligned}
\mathfrak{g}_1(u_1) &= 1 + \xi_1(u_1, \xi_2), \\
\mathfrak{g}_2(u_2) &= 1 - \xi_3(u_2, \xi_2), \\
\mathfrak{g}_i(u_i) &\approx 1 - \mathfrak{K}^{-1} u_i^2.
\end{aligned}
\tag{22}
$$

This results in the following equation of motion for the middle electrode,

$$
\xi_2 = \frac{(u_1)^2}{(\mathfrak{g}_1(u_1) - \xi_2)^2} - \frac{(u_2)^2}{(\mathfrak{g}_2(u_2) + \xi_2)^2}. \tag{23}
$$

A similar strategy can be applied for the situation with the additional coupling (see [6], Online source 4, sec. 5.5). The structure of the two electrostatic gaps becomes for this case,

$$
\mathfrak{g}_1 - \xi_2 = 1 + \xi_1 - \xi_2 \approx 1 - \tilde{g}_u \cdot u_1^2 - \tilde{g}_a \cdot u_1^2 \xi_2 - \tilde{C} \cdot \xi_2 \tag{24}
$$

and

$$
\mathfrak{g}_2 + \xi_2 = 1 - \xi_3 + \xi_2 \approx 1 - \tilde{g}_u \cdot u_2^2 + \tilde{g}_a \cdot u_2^2 \xi_2 + \tilde{C} \cdot \xi_2. \tag{25}
$$

Depending on the sign of $\tilde{g}_a$, this term may counteract the term proportional to $\tilde{g}_u$. For the push-pull NED actuator this counteracting behaviour was observed in FEM-simulations by the relative electrode motion with a single-sided drive (see [6],Online Source 4, sec. 6.3).

2.3 Stability analysis of the single-sided drive ($u_1 = u$, $u_2 = 0$)

In this section the pull-in of the single-sided reference model without coupling (fig. 4 a) is analysed in order to evaluate its dependency on the gap. The stability of the equilibrium positions is analysed by the Hesse matrix of the potential energy. If all eigenvalues are positive, this is a potential minimum, which is interpreted as stable. The reference model has more than one degree of freedom. Therefore, saddles in the potential energy can also occur. Figure 5 shows the equilibrium positions for the two actuated electrodes as well as the gaps for a single-sided drive.

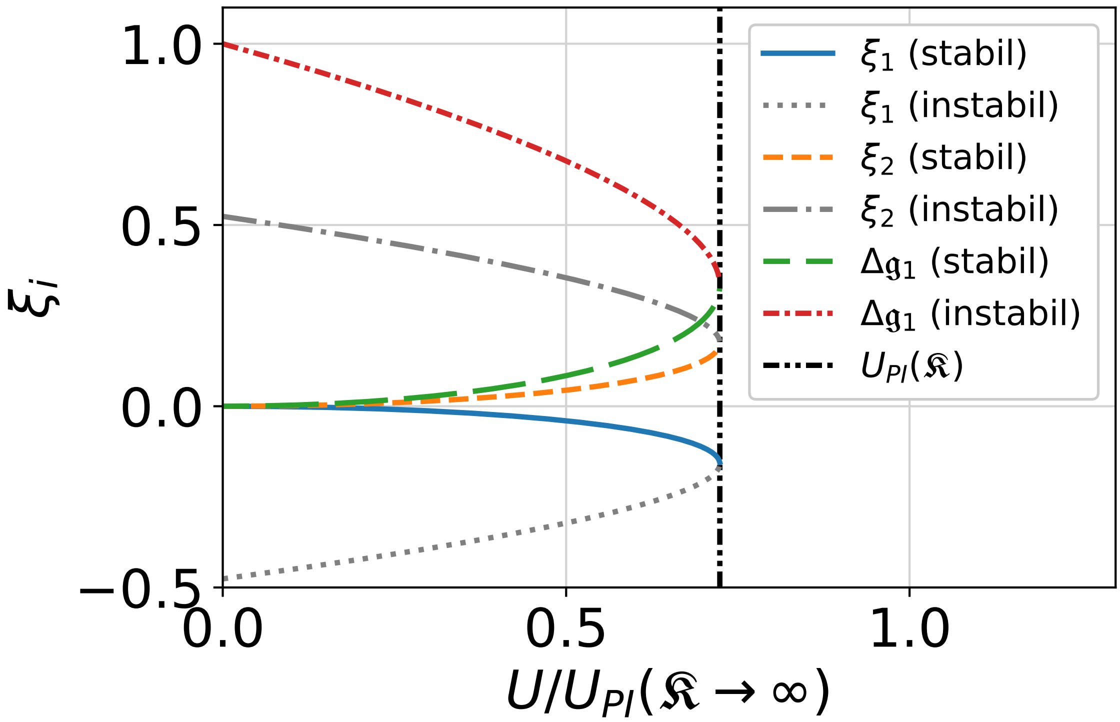

Figure 5: Electrode motion of the reference model (figure 4) with a single-sided drive

For the single-sided drive the 3-DOF model reduces to a 2-DOF model. The force equilibrium is

$$\begin{pmatrix} F_1 \\ F_2 \end{pmatrix} = \begin{pmatrix} \frac{\partial\psi}{\partial\xi_1} \\ \frac{\partial\psi}{\partial\xi_2} \end{pmatrix} = \begin{pmatrix} \mathfrak{K}\xi_1 + \frac{u_1^2}{(1+\xi_1-\xi_2)^2} \\ \xi_2 - \frac{u_1^2}{(1+\xi_1-\xi_2)^2} \end{pmatrix} = 0. \tag{26}$$

To reach equations for the pull-in voltage the relative motion of the electrodes instead of their deflection is analysed. No additional external forces are applied to the systems. Thus, the centre of mass stays unchanged. The relative motion between the upper and the middle electrode is

$$\Delta\mathfrak{g}_1 = \xi_1 - \xi_2. \tag{27}$$

The force equilibrium in equation 26 can be combined

$$0 = \frac{F_1}{\mathfrak{K}} - F_2 \tag{28}$$

to get an equation for the relative motion

$$\Delta\mathfrak{g}_1 = \left(1 + \frac{1}{\mathfrak{K}}\right) \frac{u_1^2}{(1 + \Delta\mathfrak{g}_1)^2}. \tag{29}$$

The mathematical structure of this equation is the same as for a spring-plate model with only one moveable electrode,

$$a = \frac{u^2}{(1-a)^2}, \tag{30}$$

but with a scaled voltage. The pull-in voltage of a 1-DOF model with fixed outer electrodes ($\mathfrak{K} \to \infty$) is related to the pull-in voltage with moveable outer electrodes by a scaling with the stiffness ratio $\mathfrak{K}$,

$$u_{1,\mathrm{PI}}(\mathfrak{K}, u_2 = 0) = u_{1,\mathrm{PI}}(\mathfrak{K} \to \infty, u_2 = 0) \cdot \sqrt{\frac{\mathfrak{K}}{\mathfrak{K}+1}}. \tag{31}$$

By e.g. the condition [12],

$$\frac{du}{da} = 0 \tag{32}$$

for equation 30 the dimensionless pull-in voltage with fixed outer electrodes is given by

$$u = u_{1,\mathrm{PI}}(\mathfrak{K} \to \infty, u_2 = 0) = \sqrt{\frac{4}{27}}. \tag{33}$$

Thus, the pull-in voltage for the reference model is related to the gap only by the voltage scaling,

$$U_{\mathrm{PI}} = u_{\mathrm{PI}} \cdot U_0 = g_0^{3/2} \cdot u_{\mathrm{PI}} \cdot \sqrt{\frac{2k_2}{A\epsilon_0\epsilon_r}} \tag{34}$$

2.4 Relation between gap and pull-in scaling for the reference model

1. Scaling of the dimensionless parameters
The scaling to get dimensionless quantities is given by equation 14

$$x(\tilde{\delta}_g = 0) = a \cdot g_0 \tag{35}$$

$$U(\tilde{\delta}_g = 0) = u \cdot U_0 \sim u \cdot g_0^{3/2} \tag{36}$$

2. Symmetric variation of the gap by $\tilde{\delta}_g$
The gap with a deviation $\tilde{\delta}_g$ is

$$g_{New} = g_0 \cdot (1 + \tilde{\delta}_g) \tag{37}$$

The deflection scaling in equation 35 of step one becomes

$$x(\tilde{\delta}_g) = a \cdot g_0(1 + \tilde{\delta}_g) = x(\tilde{\delta}_g = 0) \cdot (1 + \tilde{\delta}_g) \tag{38}$$

and the voltage scaling in equation 36 becomes

$$\begin{aligned} U(\tilde{\delta}_g) &\sim u \cdot g_0^{3/2} \cdot (1 + \tilde{\delta}_g)^{3/2} \\ U(\tilde{\delta}_g) &= U(\tilde{\delta}_g = 0) \cdot (1 + \tilde{\delta}_g)^{3/2} \end{aligned} \tag{39}$$

3. Relation to the pull-in scaling Υ_x and Υ_u
The scaling refers to all equilibrium positions, especially to the pull-in. Thus, the scaling of the single-sided pull-in deflection for the reference model is given by

$$\Upsilon_x = \frac{x_{\mathrm{PI}}(\tilde{\delta}_g)}{x_{\mathrm{PI}}(\tilde{\delta}_g = 0)} = \frac{a_{\mathrm{PI}} \cdot g_0 \cdot (1 + \tilde{\delta}_g)}{a_{\mathrm{PI}} \cdot g_0} = 1 + \tilde{\delta}_g \tag{40}$$

and the scaling of the pull-in voltage as

$$\Upsilon_u = \frac{U_{\mathrm{PI}}(\tilde{\delta}_g)}{U_{\mathrm{PI}}(\tilde{\delta}_g = 0)} = \frac{u_{\mathrm{PI}} \cdot g_0^{3/2} \cdot (1 + \tilde{\delta}_g)^{3/2}}{u_{\mathrm{PI}} \cdot g_0^{3/2}} = (1 + \tilde{\delta}_g)^{3/2} = \Upsilon_x^{3/2} \tag{41}$$

2.5 Reference model with a gap asymmetry

Figure 6 shows a reference model with symmetric gaps ($g_1 = g_2 = g_0$) as well as asymmetric gaps ($g_1 \neq g_2$).

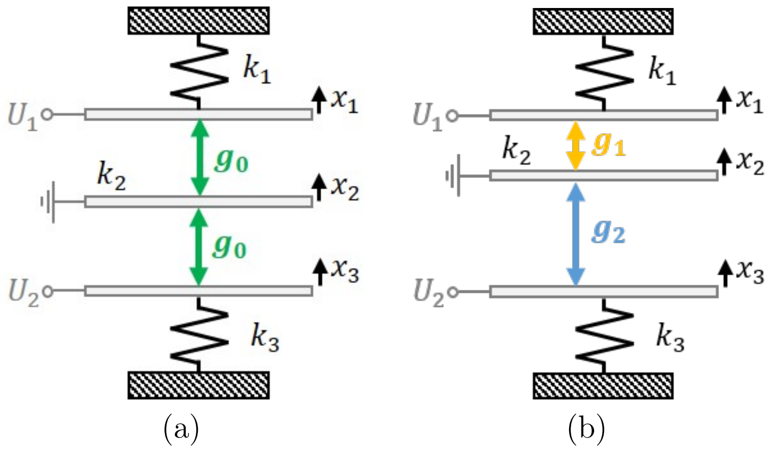

Figure 6: Reference model with symmetric gaps (a) as well as asymmetric gaps (b)

The electrostatic contribution to the potential energy V depends on the upper and lower gap,

$$V = \frac{1}{2}k_1 x_1^2 + \frac{1}{2}k_2 x_2^2 + \frac{1}{2}k_3 x_3^2 - \frac{1}{2}A\epsilon_0\epsilon_r \left(\frac{U_1^2}{g_1 + x_1 - x_2} + \frac{U_2^2}{g_2 + x_2 - x_3} \right), \tag{42}$$

with

$$\begin{aligned} g_1 &= g_0 \cdot (1 - \hat{\delta}_g), \\ g_2 &= g_0 \cdot (1 + \hat{\delta}_g). \end{aligned} \tag{43}$$

The parameter δ_g expresses the deviation from the mean for the gap. It is a dimensionless parameter. Further, with this definition the same characteristic length scale g_0 can be used to translate the deflection x into the dimensionless deflection ξ,

$$\xi = \frac{x}{g_0}. \tag{44}$$

The same definitions as in section 2.2, eq. 14 can be used to construct the dimensionless equation. The upper and lower gap in equation 23 become

$$\begin{aligned}\mathfrak{g}_1 &= 1 - \hat{\delta}_g + \xi_1, \\ \mathfrak{g}_2 &= 1 + \hat{\delta}_g - \xi_3.\end{aligned} \tag{45}$$

The approximated motion of the outer electrodes is

$$\xi_j \approx \varsigma_i \cdot \mathfrak{K}^{-1}\left(\frac{u_i}{1+\varsigma_i \cdot \hat{\delta}_g}\right)^2 \tag{46}$$

and altered by δ_g. The voltage dependent gap $\mathfrak{g}_i$ becomes

$$\mathfrak{g}_i \approx 1 - \mathfrak{K}^{-1}\left(\frac{u_i}{1+\varsigma_i \cdot \hat{\delta}_g}\right)^2. \tag{47}$$

The constants $\tilde{g}_u$ and $\tilde{g}_a$ (see 24 and 25) might thus be influenced by the additional gap asymmetry. Here, we have not further evaluated the effects, because the stability border as well as the deflection of the push-pull NED actuator are modelled already precisely by taking $g_u = g_a = 0$ also for a gap asymmetry. Other NED-actuator geometries with e.g. very shallow cells might need a careful investigation at this point. The assumption inside is that the finite stiffness of the outer electrodes and the electrode deformation by the deflection counteract each other also for geometries with an asymmetric gap. The lumped element model with an asymmetric gap becomes

$$\frac{d^2}{d\tau^2}a + \frac{1}{Q}\frac{d}{d\tau}a + a = \left(\frac{u_1}{1-\hat{\delta}_g - a}\right)^2 - \left(\frac{u_2}{1+\hat{\delta}_g + a}\right)^2. \tag{48}$$

2.6 Bifurcations of a LPM with gap asymmetry

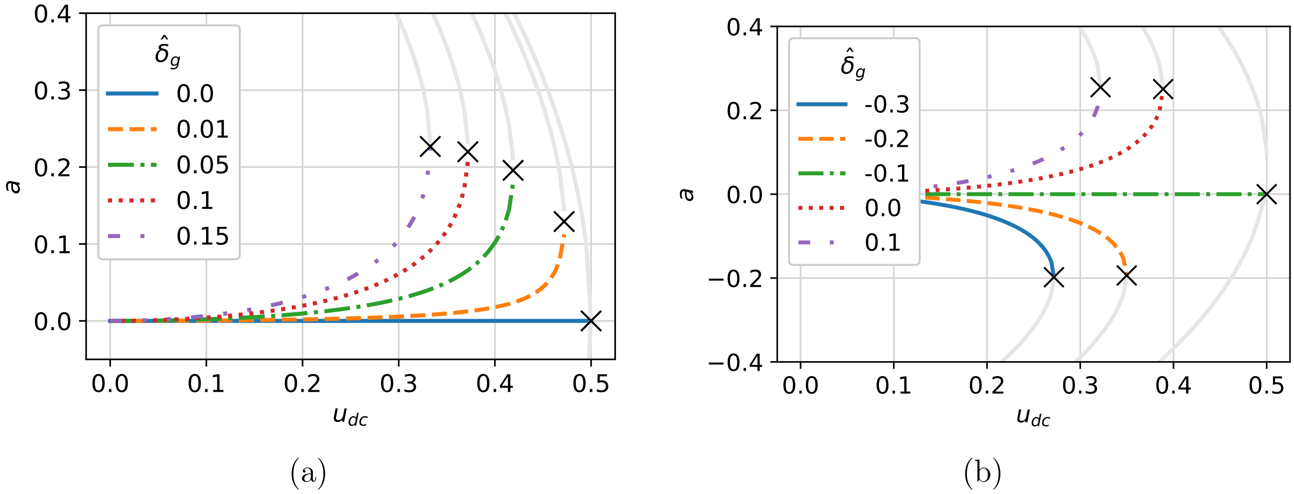

Figure 7: Stable equilibrium positions (lines) for different $\hat{\delta}_g$ with $\hat{\delta}_u = 0$ (a) and $\hat{\delta}_u = 0.1$ (b) with the pull-in (cross) and the unstable equilibria (gray lines) plotted for equation 48

3 Interpretation of the generalized degree-of-freedom a

Previously, the generalized degree-of-freedom a within the model of the push-pull NED-actuator was connected to the deflection at the actuator's tip [6]. Here we argue that the pressure signal and the deflection of the tip are linearly linked by a scaling factor. Thus, a can be interpreted either as tip deflection or as pressure signal. The sound pressure signal in units of dB is related to the root mean square of the harmonic time pressure fluctuation δp_{RMS} compared to a reference pressure of $p_{\mathrm{ref}} = 20\,\mu\mathrm{Pa}$,

$$\mathrm{SPL} = 20 \cdot \log_{10}(\frac{\delta p_{\mathrm{RMS}}}{p_{\mathrm{ref}}}). \tag{49}$$

The pressure can be obtained from the linearized adiabatic equation with the adiabatic exponent $\gamma = 1.4$, the atmospheric pressure $P_0 = 1.01 \cdot 10^5 Pa$ and the reference volume V_0,

$$\delta p_{\mathrm{RMS}} = \gamma \cdot \frac{P_0}{V_0} \frac{\delta V}{\sqrt{2}}. \tag{50}$$

The reference volume refers to the closed volume which is connected to the actuators. This volume is assumed here to have ideally no leakage. Many actuators work together in a NED microspeaker. As a first approximation, each actuator displaces the same volume (see sec. **??**). The total displaced volume is the sum of the displaced volume of a single actuator $\delta V_{\mathrm{actuator}}$ over the number of actuators $n_{\mathrm{actuators}}$,

$$\delta V = \delta V_{\mathrm{actuator}} \cdot n_{\mathrm{actuators}}. \tag{51}$$

The displaced volume is approximately the result of the swept area times the actuator height h,

$$\delta V_{\mathrm{actuator}} \approx h \cdot \delta A_{\mathrm{actuator}}. \tag{52}$$

For the push-pull NED actuator, the swept area in a stationary 2D-FEM simulation with a single-sided drive is linear with respect to the deflection at the actuator tip,

$$\delta A = 303.4\mu\mathrm{m} \cdot X_{\mathrm{Tip}}. \tag{53}$$

Figure 9 shows this connection. Figure 8 displays a schematic representation of the deflected actuator. For the swept area, the area between the edges and the neutral fiber of the actuator without actuation is subtracted from the area with actuation. The actuator shortens due to the deflection. This is maximal $0.6\,\mu\mathrm{m}$ and small compared to the deflection ($\approx 7\%$). The influence of this on the leakage at the actuator tip is not examined in more detail here.

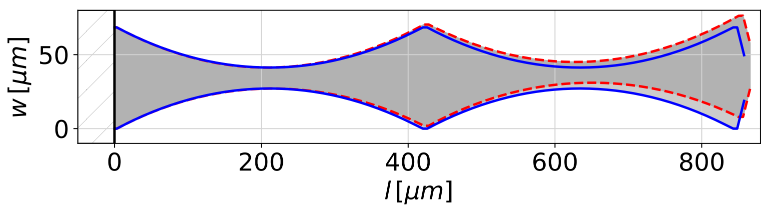

Figure 8: Initial (blue, solid) and deflected actuator (red, dashed) for a single-sided drive with a voltage of 16.4 V

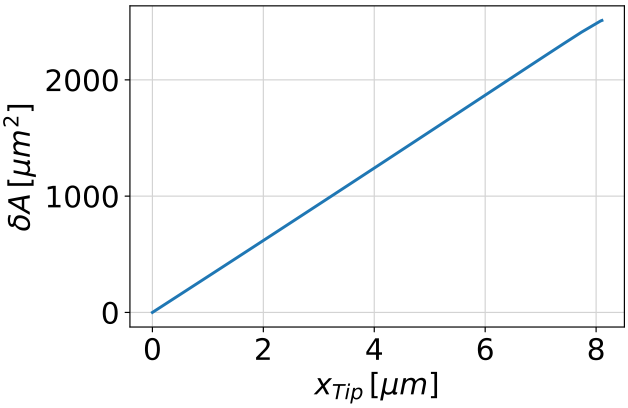

Figure 9: Linear connection between the tip deflection and the swept area for a single-sided drive

Thus, in this first approximation a scaling factor connects the deflection at the actuator tip X_{Tip}, the swept area δA and the resulting pressure p. One subtlety that must be taken into account is that if the pressure signal is to be fitted at the excitation frequency, the fundamental amplitude A_1 by a must be compared instead of the response a including all other harmonics. The dimensionless DOF can be interpreted as e.g. one of these quantities with out the need to change the dimensionless equation. The scaling between these quantities is then hidden in the scaling between the dimensionless equation and the physical properties. Other interpretations for a are also conceivable by the same logic.

4 Finite-Element-Method (FEM) simulations

4.1 Material constants

Material constants for the FEM simulations are listed in table 2 and 3. The electric field constant is $\epsilon_0 = 8{,}854 \cdot 10^{-6}\mathrm{AsV}^{-1}\mathrm{m}^{-1}$ [13]. The mechanical properties of the isolating islands between the actuator layers is set equal to silicon.

Modulus of elasticity (due to simulation approach)	E_x	10^{-9} GPa
Poisson ratio	ν_{xy}	0.
Relative electrical permittivity	ϵ	1

Table 2: Air

Modulus of elasticity	$E_{\mathrm{x}} = E_{\mathrm{y}}$ E_{z}	169 GPa 130 GPa
Poisson ratio	ν_{xz} ν_{xy} ν_{yz}	0.28 0.064 0.36
G-Modulus	$G_{\mathrm{xz}} = G_{\mathrm{yz}}$ G_{xy}	79.4 GPa 50.9 GPa
Density	ρ	$2.329\ \mathrm{g} \cdot \mathrm{cm}^{-3}$
Relative electrical permittivity	ϵ	11.68

Table 3: (100)-Silicon [14], [15], [16]

4.2 Geometry and mesh strategy

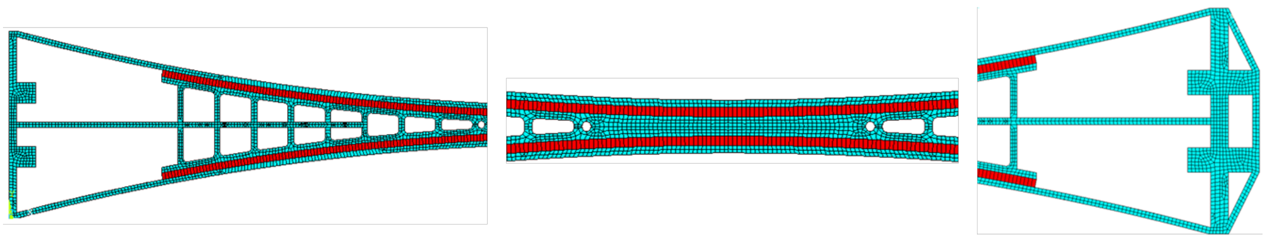

Figure 10: Mesh for the ideal geometry whereby light blue regions refer to silicon and red regions to the gap region with electrostatics [6] reproduced with premission from Springer Nature[1]

The element size is chosen small enough to ensure that deviations between the LPM and the FEM have no numerical reason ([6], Online Source 4). The symmetry of the actuator was taken into account for the mesh. This is especially important for the symmetric driving ($u_1 = u_2$). Because asymmetries lower the pull-in voltage of this driving scheme regardless of whether they have a physical meaning (e.g. gap asymmetries) or not (e.g. mesh asymmetries). First, partial regions are meshed, which are then copied, mirrored and placed together (fig. 11). For an asymmetric gap the partial region needs to be larger. Here it is chosen as half of a NED cell (fig. 12).

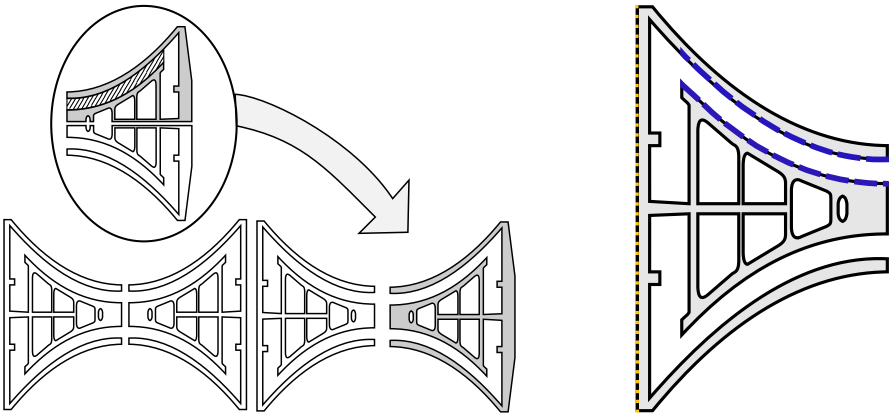

(a) (b)

Figure 11: Mesh strategy for a symmetric push-pull NED actuator starting with a quarter NED cell and their mesh (a). This region is step by step copied and mirrored to build the complete actuator. The electrostatic force is treated within the hatched gap region (a), the yellow dotted line marks the fixed boundary (b) and the electrostatic boundary conditions are applied at the dashed line (b).

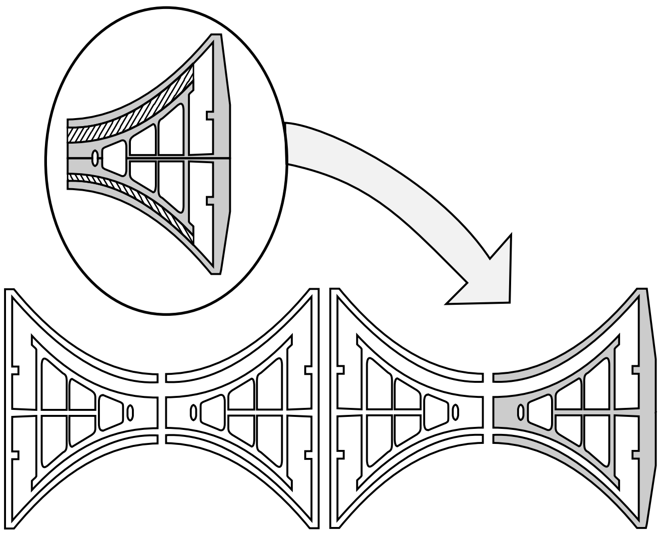

Figure 12: Adopted meshing strategy for actuators with an asymmetric gap

4.3 Pull-in estimation by FEM

While the LPM represents e.g. the tip deflection, it is not directly clear if the pull-in can be estimated by the relationship between voltage and tip deflection and how the tip deflection is related to the electrode motion within the NED cells. First, the pull-in voltage is estimated by the resonance frequency shift. The stationary deflection of a 2D-FEM model of the actuator is solved and at each equilibrium position a modal analysis is done (similar to [17]). The root of the resonance frequency is interpreted as the critical pull-in point [18].

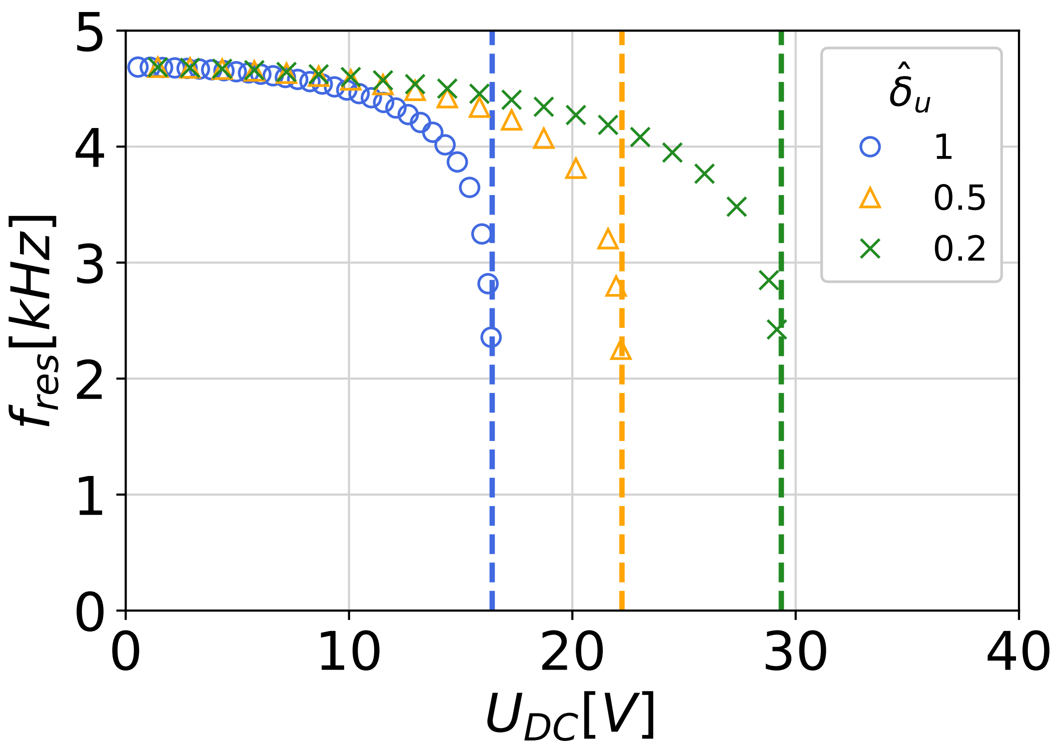

Figure 13: Resonance frequency shift of the push-pull NED actuator for an asymmetric driving by a modal 2D-FEM simulation (symbols) compared to the maximal voltage for a stationary 2D-FEM simulation with the arclength-solver (lines)

In order to estimate the pull-in of the push-pull NED-actuator, the deflection is simulated with a stationary 2D-FEM simulation in combination with an arclength-solver. The maximal reachable voltage is equal to the pull-in voltage (fig. 14) by the modal analysis (fig. 13). Thus, the pull-in voltage is identified here by analysing the tip deflection in order to reduce the simulation effort, which is higher for the combination of stationary and modal simulations (fig. 13).

The deflection of the middle electrode in the NED cell's centre x_2 is superimposed by the deflection of the actuator. Thus, the relative electrode motion is additionally analysed. $\Delta g_1 - \Delta g_2$ can be interpreted as $2 \cdot x_2$ if the motion of the outer electrodes is negligible (compare eq. 17 and 18,fig. 16). The tip deflection is only related to the motion of the middle electrode x_2 for equilibrium positions for which both NED cells behave similar (fig. 14 a and c). Two different kinds of configurations can be found. Initially both cells behave similar, meaning e.g. that both upper gaps Δg_1 decrease while the lower gaps Δg_2 increase (fig. 14 d) and $\Delta g_{1,cell1} \approx \Delta g_{1,cell2}$. In figure 15 a and b regions with a similar gap behaviour are marked. Configuration a is found in the stable region below the pull-in voltage. This region is analysed

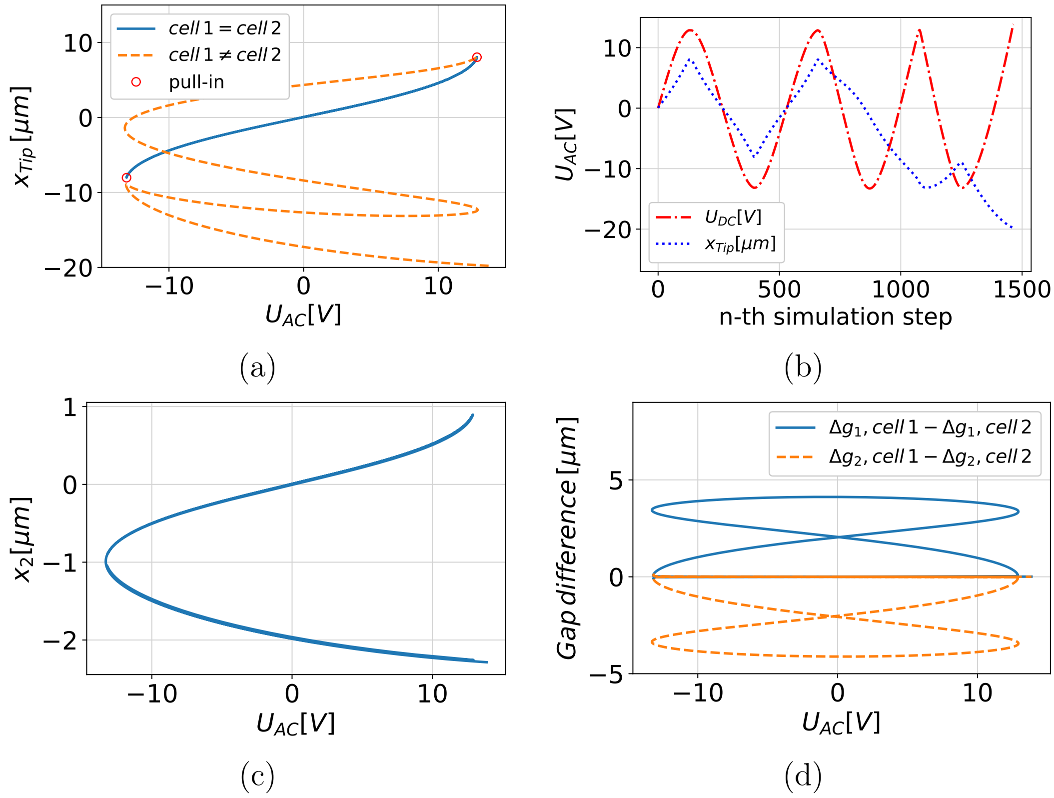

Figure 14: Tip deflection for a differential drive with $U_{\mathrm{DC}} = 20\,\mathrm{V}$ (a) as well as deflection and voltages for the n-th simulation step (b), deflection of the middle electrode within the first NED cell (c) as well as difference between gap in the first and the second NED-cell for the upper and lower layer (d) by a static 2D-FEM simulation with an arclength solver

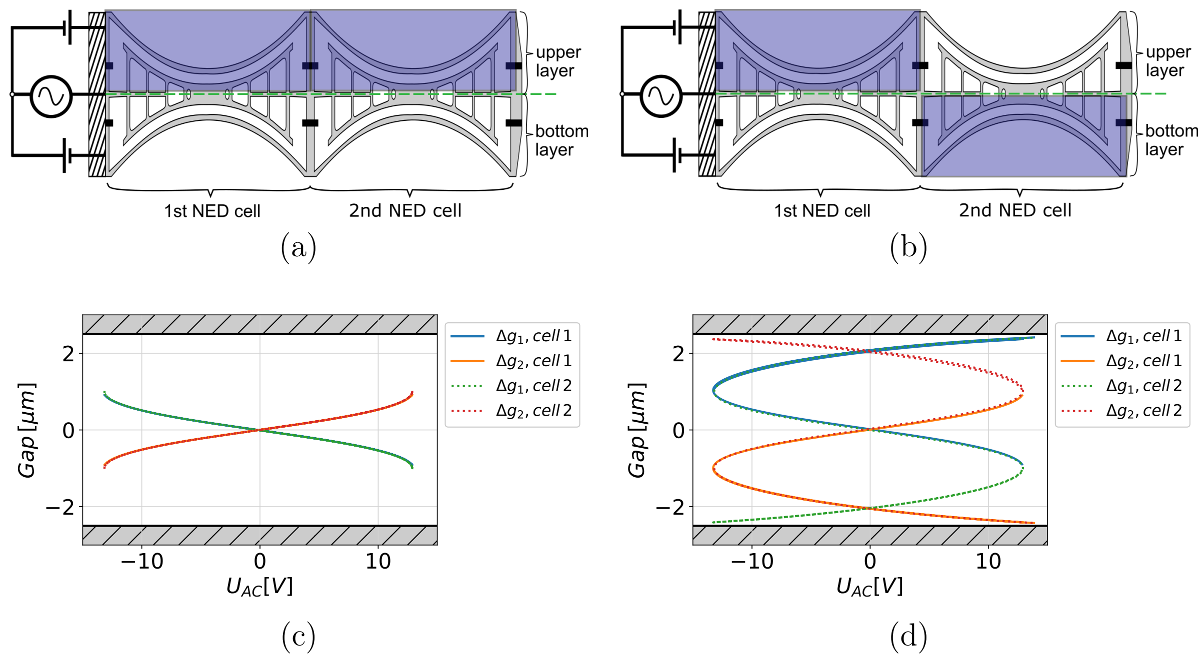

Figure 15: Gap for regions with same behaviour of both NED cells (a, c) and with different behaviour (b, d)

here and used as motivation for the LPM, which is compared to FEM simulations.

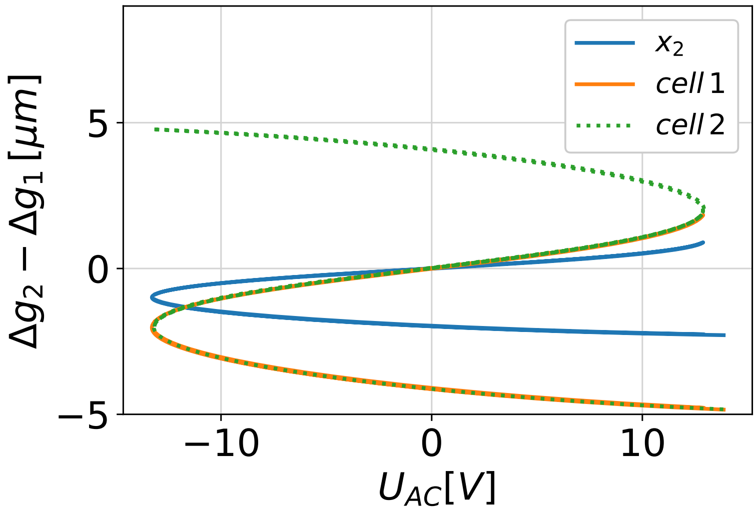

Figure 16: Difference between the upper and lower gap for the two NED-cells compared to the deflection at the middle electrode in the centre of the first NED cell with a differential drive and a bias voltage of $U_{\mathrm{DC}} = 20\,\mathrm{V}$

4.4 Normalization towards the pull-in

4.4.1 Symmetric geometry variations

Symmetric geometry variations for the push-pull NED-actuator may vary the pull-in significantly ($\lesssim \pm 40\%$ for the pull-in voltage by $\tilde{\delta}_g < 0.3$, fig. 4) but seem to have at the same time a small influence on the dimensionless model structure. Figure 19 shows the tip deflection in a stationary 2D-FEM simulation by a differential driving for a variation of the bias voltage with a constant signal-to-bias-ratio normalized to the respective pull-in. The relative deviation RE is below 2%. Note, the FEM-simulations are not dimensionless. The different curves are not all exactly solved for the same dimensionless voltages. Thus, a cubic interpolation is used to calculate the difference between the ideal geometry and simulations with symmetric tolerances for the normalized curves. Compared to the large deviation of the pull-in values itself, this relative error for the curve shape is small. Further, the pull-in border for a differential drive is evaluated dimensionless. Figure 17 shows the quasi-static pull-in voltage normalized to the single-sided pull-in voltage. The relative deviation between the ideal structure and geometries with a symmetric gap variation is below 0.03%. In a dimensionless form, the shape of the pull-in border is nearly unaffected by symmetric gap variations. A similar behaviour is observed for a symmetric variation of the outer electrode thickness $\tilde{\delta}_b$ (fig. 18 based on [8]).

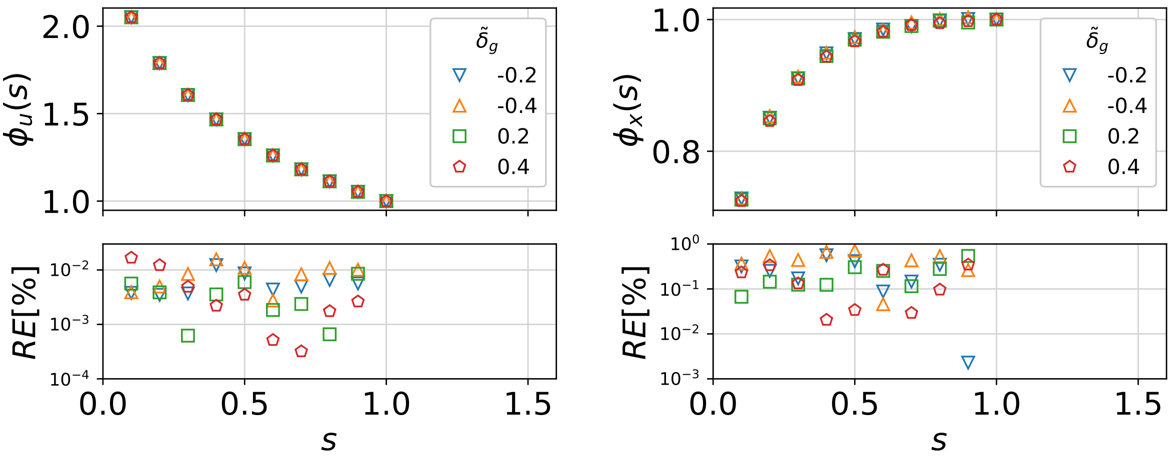

(a) (b)

Figure 17: Pull-in border $\phi_u(s)$ and $\phi_x(s)$ by stationary 2D-FEM simulations normalized to the single-sided pull-in for gap variations as well as the relative deviation RE between the 2D-FEM simulation of an ideal geometry and simulations with symmetric gap tolerances $\tilde{\delta}_g$

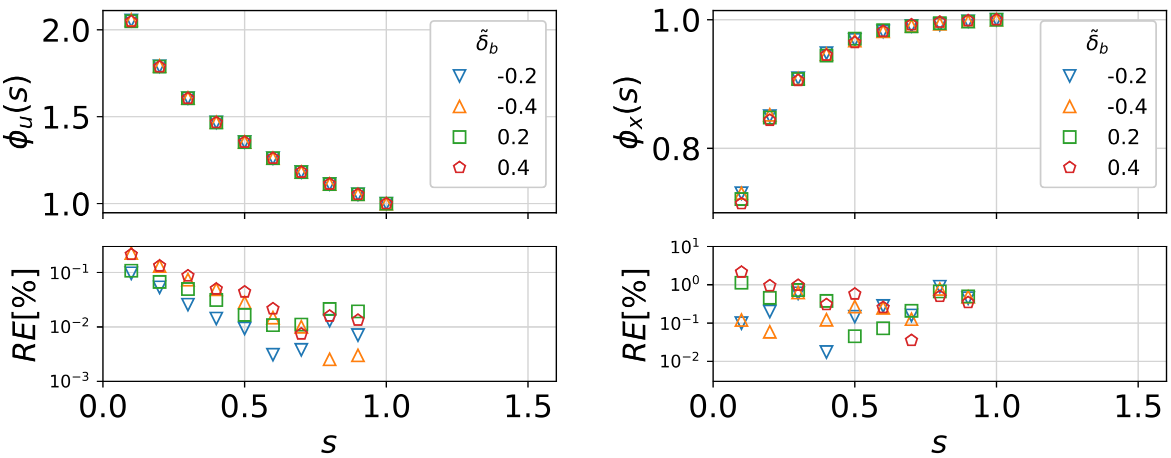

(a) (b)

Figure 18: Pull-in border $\phi_u(s)$ and $\phi_x(s)$ by stationary 2D-FEM simulations normalized to the single-sided pull-in for gap variations as well as the relative deviation RE between the 2D-FEM simulation of an ideal geometry and simulations with symmetric tolerances of the outer electrode thickness $\tilde{\delta}_b$ based on [8]

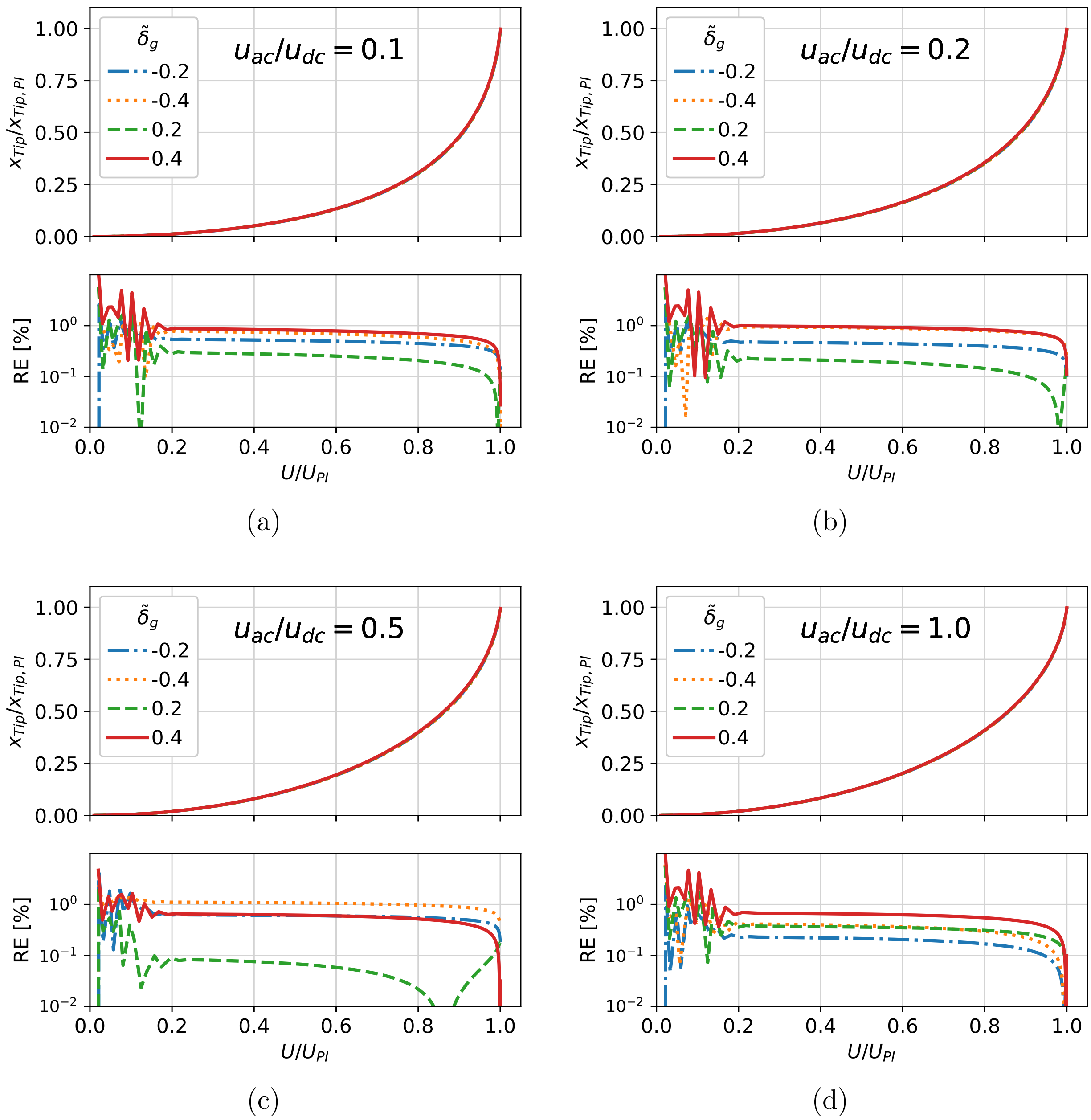

Figure 19: Voltage-deflection curves by stationary 2D-FEM simulations with a differential driving normalized to the pull-in for different symmetric gap variations $\tilde{\delta}_g$ and signal- to bias-ratios u_{ac}/u_{dc} (a: 0.1, b: 0.2, c: 0.5, d:1.0) as well as the relative error between simulations with $\tilde{\delta}_g$ and the ideal actuator geometry

4.4.2 Asymmetric geometry variations

In contrast to symmetric geometry variations, the pull-in normalized voltage-deflection curves differ if e.g. an asymmetric gap is simulated (figure 20). The deviation depends on the working point. For a single-sided drive (equivalent to a differential drive with $u_{\mathrm{ac}}/u_{\mathrm{dc}} = 1$) the gap asymmetry has nearly no impact on the curve shape for $\hat{\delta}_g = 0.3$. The curve shape seems to be dominated by the active layer.

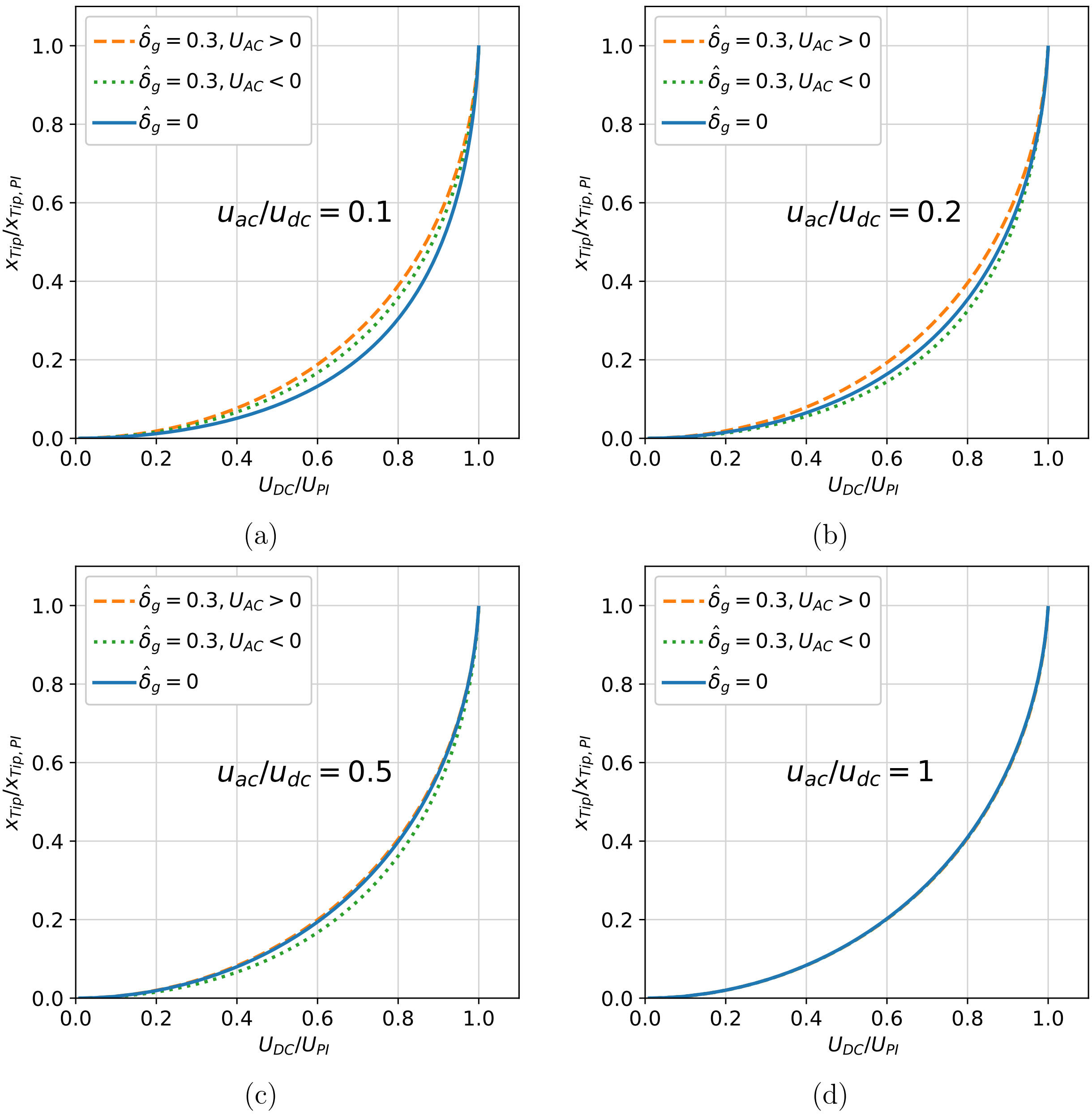

Figure 20: Normalized voltage-deflection curves of a 2D-FEM simulation for the ideal geometry $\hat{\delta}_g = 0$ as well as a gap asymmetry of $\hat{\delta}_g = 0.3$ for a differential drive with a variation of the bias voltage and a fixed signal-to-bias ratios u_{ac}/u_{dc} (a: 0.1, b: 0.2, c:0.5, d:1.0)

5 The push-pull microspeaker

5.1 Principle of the microspeaker device

The microspeaker consists out of the cover and bottom wafer with venting holes and a device plane with the actuators. Figure 21 gives a scheme of the top and side view.

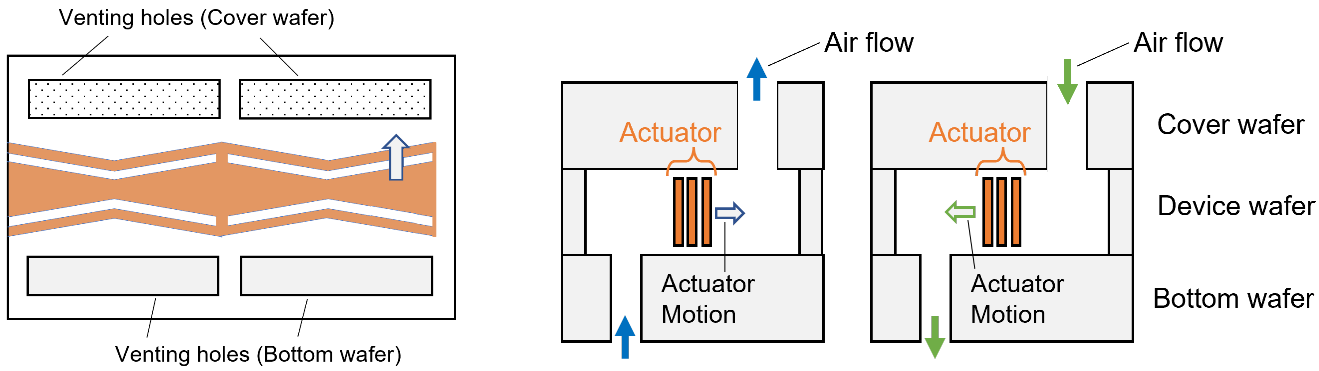

(a) (b) (c)

Figure 21: Working principle of the investigated microspeaker with push-pull NED actuators within a cavity deflecting in two opposing directions as top view (a) and side view (b, c)

5.2 MEMS Device

Each microspeaker chip (fig. 22 a) is divided into two halfs with the same bias voltage at the outer electrodes for each. Each half is divided into 12 rows with 10 actuators per row. Actuator rows are selected by the applied AC signal. Summed up, 240 actuators are placed on the chip. The chip is placed on a printed circuit boeard (PCB) and connected with bond wires. Deatails about the actuator and its fabrication can be found in [10].

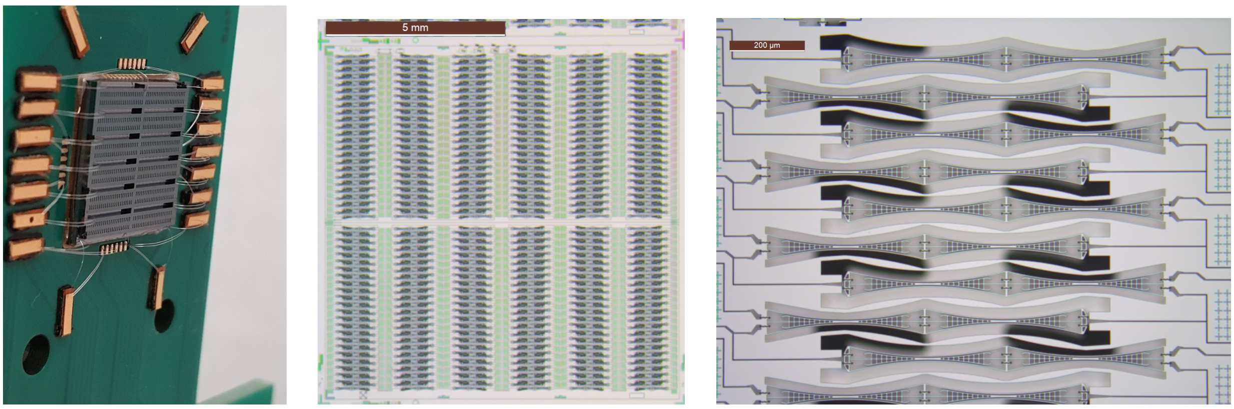

(a) (b) (c)

Figure 22: MEMS loudspeaker on PCB with wire bonds (a), device wafer with several NED actuators (b) as well as detailed image of the device wafer

6 Flowcharts and recipes for the LPM predictions

6.1 U_0 and X_0 by FEM

Besides the distortion analysis of [6] the voltage and length scale can be evaluated by a stationary FEM simulation with a single-sided drive (fig. 23). The simulation effort is less for this second strategy in terms of number of necessary FEM-simulations. From the experimental point this would refer to the destructive pull-in evaluation of a single actuator.

1. Define geometry ($\tilde{\delta}_g = 0, \hat{\delta}_g = 0$), single-sided drive ($U_2$=0)

stationary FEM with arclength solver,
if necessary additional modal analysis to identify the pull-in (see sec. 4.3)

2. Pull-in voltage $U_{1,\mathrm{PI}}(U_2 = 0)$,
pull-in deflection $X_{PI}(U_1 = U_{1,\mathrm{PI}}, U_2 = 0)$

$+$

3. Evaluate LPM Pull-in

$$a = \frac{u_1^2}{(1-a)^2} \Rightarrow u_{1,PI}(u_2 = 0) = \sqrt{\frac{4}{27}},\ a_{PI}(u_1 = u_{1,PI}, u_2 = 0) = \frac{1}{3} \tag{54}$$

4. Result: Length and voltage scaling

$$\begin{aligned} U_0 &= \frac{U_{1,PI}(U_2 = 0)}{u_{1,PI}(u_2 = 0)} \\ X_0 &= \frac{X_{1,PI}(U_1 = U_{1,PI}, U_2 = 0)}{X_{PI}(u_1 = u_{1,PI}, u_2 = 0)} \end{aligned} \tag{55}$$

Figure 23: Determining the length and voltage scaling for the ideal actuator geometry

6.2 U_0 and X_0 by harmonic distortions analysis

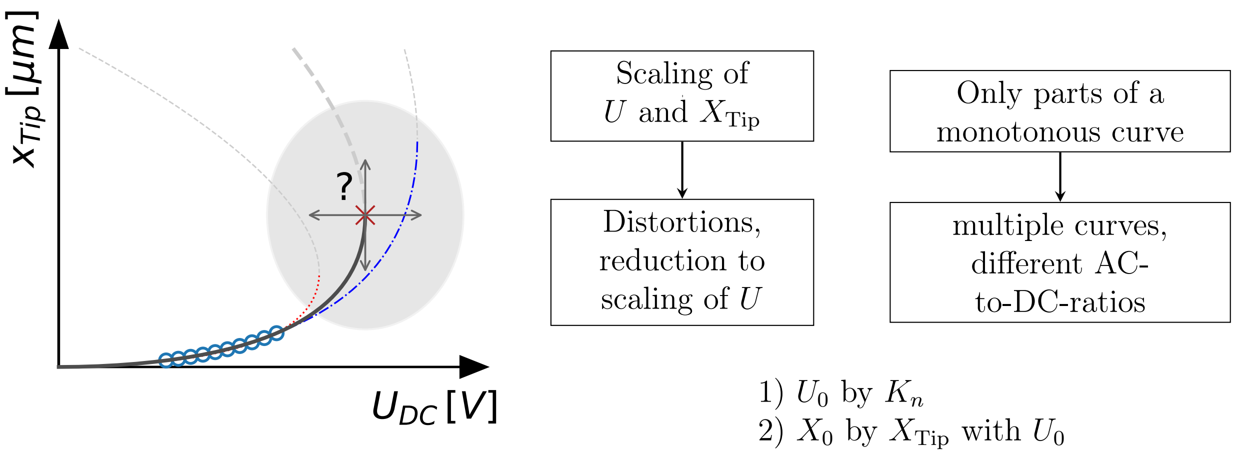

(a) (b)

Figure 24: Challenge (a) to estimate the static pull-in (cross) by measurements/simulations (circles) at low voltages by a dimensionless model (line) as well as a possible solution strategy (b)

Figure 24 summarized the challenge to relate a dimensionless equation to the voltage-deflection-curve at low voltages to estimate the voltage scaling U_0 as well as a possible solution strategy. The first step, the estimation of the pull-in voltage by the third harmonic K_3 with a differential drive is documented in detail in [6]. The voltage scaling, which is directly related to the pull-in voltage, is estimated by K_3 for the quasi-static limit at various signal-to-bias-ratios for a differential drive. Next, the tip deflection X_{Tip} is evaluated at low voltages. Thereby, the scaling of the dimensionless degree-of-freedom a,

$$X_{\mathrm{Tip}} = X_0 \cdot a. \tag{56}$$

is inserted into the dimensionless model

$$\frac{X_{\mathrm{Tip}}}{X_0} = \frac{\left(\frac{U_{\mathrm{DC}}}{U_0}\right)^2 \left(1 + \frac{U_{\mathrm{AC}}}{U_{\mathrm{DC}}}\right)^2}{\left(1 - \frac{X_{\mathrm{Tip}}}{X_0}\right)^2} - \frac{\left(\frac{U_{\mathrm{DC}}}{U_0}\right)^2 \left(1 - \frac{U_{\mathrm{AC}}}{U_{\mathrm{DC}}}\right)^2}{\left(1 + \frac{X_{\mathrm{Tip}}}{X_0}\right)^2} \tag{57}$$

leaving X_0 as fit parameter for the curves in figure 25 a. The relative deviation is below 1% for $X_0 = 27.5\,\mu\mathrm{m}$. Figure 25 b shows a comparison of equation 57 with $U_0 = 86.06\,\mathrm{V}$ and $X_0 = 27.5\,\mu\mathrm{m}$ with 2D-FEM simulations for a differential drive with different bias voltages for the ideal actuator geometry for larger voltages up to the pull-in voltage.

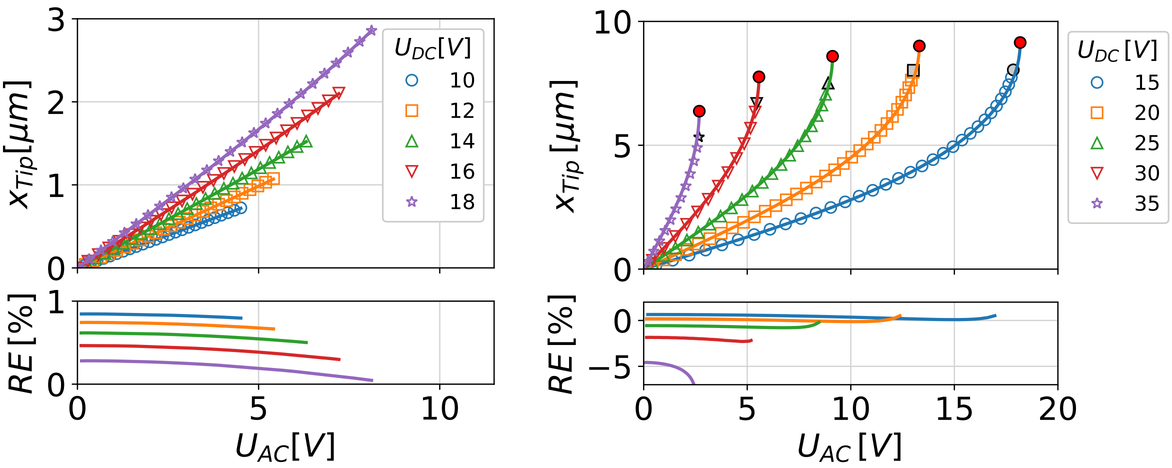

(a) (b)

Figure 25: Parameter estimation for the deflection scaling $X_0 = 27.5\,\mu\text{m}$ with small driving voltages compared to the pull-in voltage (a) as well as tip deflection by 2D-FEM simulations (symbols) compared to the LPM (lines). RE refers to the relative error between the FEM simulations and the LPM. The FEM pull-in is marked with grey filled symbols and the pull-in of the LPM is indicated by red-filled symbols.

6.3 Adjusted length and voltage scaling by symmetric geometry variations with FEM

A symmetric geometry variation can be treated by the recipe in sec. 6.1 be replacing $\tilde{\delta}_g = 0$ with a value $\tilde{\delta}_g \neq 0$. With this, one FEM simulation is necessary per geometry variation to determine the corresponding length and voltage scaling. For instance, Monte-Carlo simulations might require large sets of different geometry variations. Thus, it could be beneficial to interpret the geometry variation as an additional length and voltage scaling, Υ_x and $_u$,respectively, with respect to the ideal geometry.

Aim: $\Upsilon_u(\tilde{\delta}_g)$ and $\Upsilon_x(\tilde{\delta}_g)$ by FEM-simulations

1. Set the value range for $\tilde{\delta}_g \in [\tilde{\delta}_{g,min}, \tilde{\delta}_{g,max}]$

2. Check normalized pull-in border for $\tilde{\delta}_{g,min}$ and $\tilde{\delta}_{g,max}$ (see sec. 4.4)

3. Select supporting points out of $[\tilde{\delta}_{g,min}, \tilde{\delta}_{g,max}]$

Repeat for each supporting point $\tilde{\delta}_{g,i}$

4. Define geometry with symmetric $\tilde{\delta}_{g,i}$, single-sided drive (U_2=0)

stationary FEM with arclength solver,
if necessary additional modal analysis to identify the pull-in (see sec. 4.3)

5. Pull-in voltage $U_{1,\mathrm{PI}}(U_2 = 0, \tilde{\delta}_g = \tilde{\delta}_{g,i})$,
pull-in deflection $x_{PI}(U_1 = U_{1,\mathrm{PI}}, U_2 = 0, \delta_g = \delta_{g,i}))$

+

6. Evaluate single-sided pull-in of the ideal geometry (sec. 6.1)
$\Rightarrow U_{1,\mathrm{PI}}(U_2 = 0, \delta_g = 0)$, $x_{PI}(U_1 = U_{1,\mathrm{PI}}, U_2 = 0, \delta_g = 0))$

7. Length and voltage scaling by symmetric geometry variation

$$\begin{aligned}\Upsilon_u(\tilde{\delta}_{g,i}) &= \frac{U_{1,PI}(U_2 = 0, \tilde{\delta}_g = \tilde{\delta}_{g,i})}{U_{1,PI}(U_2 = 0, \tilde{\delta}_g = 0)} \\ \Upsilon_x(\tilde{\delta}_{g,i}) &= \frac{x_{1,PI}(U_2 = 0, \tilde{\delta}_g = \tilde{\delta}_{g,i})}{x_{1,PI}(U_2 = 0, \tilde{\delta}_g = 0)}\end{aligned} \tag{58}$$

8. Use a polynomial fit or interpolation based on all $\Upsilon_u(\tilde{\delta}_{g,i})$ and $\Upsilon_x(\tilde{\delta}_{g,i})$

9.Result: $\Upsilon_u(\tilde{\delta}_g)$ and $\Upsilon_x(\tilde{\delta}_g)$ for the chosen value range of $\tilde{\delta}_g$

Figure 26: Determining the additional length and voltage scaling for symmetric geometry variations

6.4 Pull-in border for a symmetric actuator with a differential drive

Figure 27 gives the main steps to determine the pull-in border for a symmetric actuator. Up to two FEM-simulations are necessary for this estimation. The length and voltage scaling is determined by section 6.1. The impact by a geometry variation can be determined by section 6.3. If multiple geometry variations are evaluated, e.g. to rate an actuator ensemble, few simulations like in section 6.3 can be utilized to generate an interpolation for $\Upsilon_u(\tilde{\delta}_g)$ and $\Upsilon_x(\tilde{\delta}_g)$. Alternatively, a reference model can motivate a function for $\Upsilon_u(\tilde{\delta}_g)$ and $\Upsilon_x(\tilde{\delta}_g)$ (sec. 2.4). This could further reduce the simulation effort, but not every geometry variation allows this kind of guess.

1. Evaluate LPM pull-in border

$$a = u_{\mathrm{dc}}^2 \Big(\frac{(1+\hat{\delta}_u)^2}{(1-a)^2} - \frac{(1-\hat{\delta}_u)^2}{(1-a)^2} \Big) \Rightarrow u_{\mathrm{dc,PI}}(\hat{\delta}_u), a_{\mathrm{PI}}(u_{\mathrm{dc,PI}},\, \hat{\delta}_u) \tag{59}$$

$\downarrow$

2. Result: physical pull-in border by U_0 and X_0 (sec. 6.1) as well as $\Upsilon_u(\tilde{\delta}_g)$ and $\Upsilon_x(\tilde{\delta}_g)$ (sec. 6.3)

$$\begin{aligned} U_{\mathrm{DC,PI}}(\hat{\delta}_u, \tilde{\delta}_g) &= \Upsilon_u(\tilde{\delta}_g) \cdot U_0 \cdot u_{\mathrm{dc,PI}}(\hat{\delta}_u) \\ X_{\mathrm{PI}}(U_{\mathrm{DC,PI}}, \hat{\delta}_u, \tilde{\delta}_g) &= \Upsilon_x(\tilde{\delta}_g) \cdot X_0 \cdot a_{\mathrm{PI}}(u_{\mathrm{dc,PI}}, \hat{\delta}_u) \end{aligned} \tag{60}$$

Figure 27: Pull-in border with symmetric geometry variations

To verify the estimated pull-in border, FEM-simulations with fixed $\hat{\delta}_u$ and $\tilde{\delta}_g$ are done with a variation of U_{DC} to determine step-wise $U_{\mathrm{DC,PI}}(\hat{\delta}_u, \tilde{\delta}_g)$. Note, within the quasi-static limit $\hat{\delta}_u$ is mathematically equivalent to $\frac{U_{\mathrm{AC}}}{U_{\mathrm{DC}}}$

6.5 Pull-in border for an asymmetric actuator with a differential drive

Here, essentially three FEM-simulations are necessary. One simulation to estimate the length and voltage scaling of the ideal geometry (sec. 6.1), and two simulations to determine $\Upsilon_u(+\tilde{\delta}_g)$ and $\Upsilon_u(-\tilde{\delta}_g)$ as well as $\Upsilon_x(+\tilde{\delta}_g)$ and $\Upsilon_x(-\tilde{\delta}_g)$ (sec. 6.3). Again, by using e.g. an interpolation for $\Upsilon_u(\tilde{\delta}_g)$ and $\Upsilon_x(\tilde{\delta}_g)$ the simulation effort can be reduced if an actuator ensemble or Monte-Carlo simulations are evaluated.

1. FEM simulations to determine the length and voltage scaling

    1. ideal geomtry $\Rightarrow U_0$, X_0 (sec. 6.1)
    2. geometry with $+\tilde{\delta}_g \Rightarrow \Upsilon_u(+\tilde{\delta}_g), \Upsilon_x(+\tilde{\delta}_g)$ (sec. 6.3)
    3. geometry with $-\tilde{\delta}_g \Rightarrow \Upsilon_u(-\tilde{\delta}_g), \Upsilon_x(-\tilde{\delta}_g)$ (sec. 6.3)

2. Calculate $\dfrac{\Upsilon_x(+\tilde{\delta}_g)^3}{\Upsilon_u(+\tilde{\delta}_g)^2}$ and $\dfrac{\Upsilon_x(-\tilde{\delta}_g)^3}{\Upsilon_u(-\tilde{\delta}_g)^2}$

3. Evaluate LPM pull-in border for

$$a = \frac{\Upsilon_x(-\tilde{\delta}_g)^3}{\Upsilon_u(-\tilde{\delta}_g)^2} \cdot \frac{u_1^2}{(\Upsilon_x(-\tilde{\delta}_g) - a)^2} - \frac{\Upsilon_x(+\tilde{\delta}_g)^3}{\Upsilon_u(+\tilde{\delta}_g)^2} \cdot \frac{u_2^2}{(\Upsilon_x(+\tilde{\delta}_g) + a)^2} \tag{61}$$

$\Rightarrow u_{\mathrm{DC,PI}}(\hat{\delta}_u, \hat{\delta}_g), a_{\mathrm{PI}}(u_{\mathrm{DC,PI}}, \hat{\delta}_u, \hat{\delta}_g)$

4. Result: physical pull-in border

$$\begin{aligned} U_{\mathrm{DC,PI}}(\hat{\delta}_u, \hat{\delta}_g) &= U_0 \cdot u_{\mathrm{DC,PI}}(\hat{\delta}_u, \hat{\delta}_g) \\ X_{\mathrm{DC,PI}}(\hat{\delta}_u, \hat{\delta}_g) &= X_0 \cdot a_{\mathrm{DC,PI}}(\hat{\delta}_u, \hat{\delta}_g) \end{aligned} \tag{62}$$

Figure 28: Pull-in border with asymmetric geometry variations

6.6 Deflection with symmetric geometry variations

Note, within the quasi-static limit $\hat{\delta}_u$ is mathematically equivalent to $\dfrac{U_{\mathrm{AC}}}{U_{\mathrm{DC}}}$.
The same strategy is possible for other driving schemes. The corresponding input voltages are scaled in step two and inserted within the LPM for u_1 and u_2 in step three.

1. Determine the length and voltage scaling

   1. ideal geomtry $\Rightarrow U_0$, X_0 by harmonic distortion analysis (sec. 6.2))
   2. geometry with $\tilde{\delta}_g \Rightarrow \Upsilon_u(\tilde{\delta}_g)$,$\Upsilon_x(\tilde{\delta}_g)$ (sec. 6.3)

2. Scale input voltage: $u_{\mathrm{dc}} = \dfrac{U_{\mathrm{DC}}}{\Upsilon_u(\tilde{\delta}_g) \cdot U_0}$

3. Evaluate $a(u_{\mathrm{dc}}, \hat{\delta}_u)$ by the roots for

$$a - u_{\mathrm{dc}}^2 \frac{(1+\hat{\delta}_u)^2}{(1-a)^2} + u_{\mathrm{dc}}^2 \frac{(1-\hat{\delta}_u)^2}{(1+a)^2} = 0 \Rightarrow a(u_{\mathrm{dc}}, \hat{\delta}_u) \tag{63}$$

4. Result: Deflection

$$X(U_{\mathrm{DC}}, \hat{\delta}_u, \tilde{\delta}_g) = \Upsilon_x(\tilde{\delta}_g) \cdot X_0 \cdot a(u_{\mathrm{dc}}, \hat{\delta}_u) \tag{64}$$

Figure 29: Deflection with symmetric geometry variations

6.7 Deflection with asymmetric geometry variations

Note, within the quasi-static limit $\hat{\delta}_u$ is mathematically equivalent to $\dfrac{U_{\mathrm{AC}}}{U_{\mathrm{DC}}}$.
The same strategy is possible for other driving schemes. The corresponding input voltages are scaled in step three and inserted within the LPM for u_1 and u_2 in step four.

1. Determine the length and voltage scaling

    1. ideal geomtry $\Rightarrow U_0$, X_0 by harmonic distortion analysis (sec. 6.2))
    2. geometry with $+\tilde{\delta}_g \Rightarrow \Upsilon_u(+\tilde{\delta}_g), \Upsilon_x(+\tilde{\delta}_g)$ (sec. 6.3)
    3. geometry with $-\tilde{\delta}_g \Rightarrow \Upsilon_u(-\tilde{\delta}_g), \Upsilon_x(-\tilde{\delta}_g)$ (sec. 6.3)

2. Calculate $\dfrac{\Upsilon_x(+\tilde{\delta}_g)^3}{\Upsilon_u(+\tilde{\delta}_g)^2}$ and $\dfrac{\Upsilon_x(-\tilde{\delta}_g)^3}{\Upsilon_u(-\tilde{\delta}_g)^2}$

3. Scale input voltage: $u_{\mathrm{dc}} = \dfrac{U_{\mathrm{DC}}}{U_0}$

4. Evaluate $a(u_{\mathrm{dc}}, \hat{\delta}_u, \hat{\delta}_g)$ by the roots for

$$a - \frac{\Upsilon_x(-\tilde{\delta}_g)^3}{\Upsilon_u(-\tilde{\delta}_g)^2} \cdot u_{\mathrm{dc}}^2 \frac{(1+\hat{\delta}_u)^2}{(\Upsilon_x(-\tilde{\delta}_g) - a)^2} + \frac{\Upsilon_x(+\tilde{\delta}_g)^3}{\Upsilon_u(+\tilde{\delta}_g)^2} \cdot u_{\mathrm{dc}}^2 \frac{(1-\hat{\delta}_u)^2}{(\Upsilon_x(+\tilde{\delta}_g) + a)^2} = 0 \Rightarrow a(u_{\mathrm{dc}}, \hat{\delta}_u) \tag{65}$$

with $\tilde{\delta}_g = \hat{\delta}_g$

5. Result: Deflection

$$X(U_{\mathrm{DC}}, \hat{\delta}_u, \hat{\delta}_g) = X_0 \cdot a(u_{\mathrm{dc}}, \hat{\delta}_u, \hat{\delta}_g) \tag{66}$$

Figure 30: Deflection with asymmetric geometry variations

References

[1] A. Bouchaala, A. H. Nayfeh, and M. I. Younis, "Frequency shifts of micro and nano cantilever beam resonators due to added masses," *Journal of Dynamic Systems, Measurement, and Control*, vol. 138, no. 9, p. 091002, 2016.

[2] M. I. Younis, *MEMS linear and nonlinear statics and dynamics*, vol. 20. Springer Science & Business Media, 2011.

[3] I. Kovacic and M. J. Brennan, *The Duffing equation: nonlinear oscillators and their behaviour*. John Wiley & Sons, 2011.

[4] Eihab M Abdel-Rahman, Mohammad I Younis, and Ali H Nayfeh, “Characterization of the mechanical behavior of an electrically actuated microbeam,” *Journal of Micromechanics and Microengineering*, vol. 12, no. 6, p. 759, 2002.

[5] M. I. Younis, E. M. Abdel-Rahman, and A. Nayfeh, “A reduced-order model for electrically actuated microbeam-based mems,” *Journal of Microelectromechanical systems*, vol. 12, no. 5, pp. 672–680, 2003.

[6] F. Wall, H. A. Schenk, A. Melnikov, B. Kaiser, and H. Schenk, “A non-destructive electro-acoustic method to characterize the pull-in voltage of electrostatic actuators,” *Nonlinear Dynamics*, 2023.

[7] H. A. Schenk, A. Melnikov, F. Wall, M. Gaudet, M. Stolz, D. Schuffenhauer, and B. Kaiser, “Electrically actuated microbeams: An explicit calculation of the coulomb integral in the entire stable and unstable regimes using a chebyshev-edgeworth approach,” *Phys. Rev. Appl.*, vol. 18, p. 014059, Jul 2022.

[8] F. Wall, S. Langa, H. A. G. Schenk, A. Melnikov, J. M. Monsalve, and B. Kaiser, “Numerical study of geometry variations in a balanced mems-loudpseaker,” in *MikroSystemTechnik 2023; Congress*, pp. 651–654, VDE, 2023.

[9] A. Melnikov, H. A. Schenk, M. Stolz, A. Mrosk, L. Ehrig, F. Wall, J. M. Monsalve, M. Ahnert, S. Langa, and B. Kaiser, “Balanced mems loudspeaker: Coulomb forces vs. viscosity of air and squeeze film damping,” 2021.

[10] B. Kaiser, H. A. G. Schenk, L. Ehrig, F. Wall, J. M. Monsalve, S. Langa, M. Stolz, A. Melnikov, H. Conrad, D. Schuffenhauer, and H. Schenk, “The push-pull principle: an electrostatic actuator concept for low distortion acoustic transducers,” *Microsystems & Nanoengineering*, vol. 8, no. 1, p. 125, 2022.

[11] D. Elata and H. Bamberger, “On the dynamic pull-in of electrostatic actuators with multiple degrees of freedom and multiple voltage sources,” *Journal of Microelectromechanical systems*, vol. 15, no. 1, pp. 131–140, 2006.

[12] H. Nathanson, W. Newell, R. Wickstrom, and J. Davis, “The resonant gate transistor,” *IEEE Transactions on Electron Devices*, vol. 14, no. 3, pp. 117–133, 1967.

[13] C. on Data for Science and T. (CODATA), “Fundamental physical constants, vacuum electric permittivity.”

[14] M. A. Hopcroft, W. D. Nix, and T. W. Kenny, “What is the young’s modulus of silicon?,” *Journal of microelectromechanical systems*, vol. 19, no. 2, pp. 229–238, 2010.

[15] W. Dunlap Jr and R. Watters, “Direct measurement of the dielectric constants of silicon and germanium,” *Physical Review*, vol. 92, no. 6, p. 1396, 1953.

[16] I. Henins, “Precision density measurement of silicon,” *Journal of research of the National Bureau of Standards. Section A, Physics and chemistry*, vol. 68, no. 5, p. 529, 1964.

[17] A. Melnikov, H. A. Schenk, F. Wall, B. Spitz, L. Ehrig, S. Langa, M. Stolz, B. Kaiser, H. Conrad, and H. Schenk, “Minimization of nonlinearities in nano electrostatic drive actuators using validated coupled-field simulation,” in *MOEMS and Miniaturized Systems XIX*, vol. 11293, pp. 91–97, SPIE, 2020.

[18] W. Rust, *Nichtlineare Finite-Elemente-Berechnungen*. Springer, 2011.